Field-orientation-dependent magnetic phases in GdRu$_2$Si$_2$ probed with muon-spin spectroscopy

B. M. Huddart [1,2] A. Hernández-Melián [1] G. D. A. Wood [3] D. A. Mayoh,[3] M. Gomilšek [4,5] Z. Guguchia,[6] C. Wang,[6]
T. J. Hicken [6] S. J. Blundell [2] G. Balakrishnan [3] and T. Lancaster [1]

[1]*Department of Physics, Durham University, Durham DH1 3LE, United Kingdom*
[2]*Clarendon Laboratory, University of Oxford, Department of Physics, Oxford OX1 3PU, United Kingdom*
[3]*University of Warwick, Department of Physics, Coventry CV4 7AL, United Kingdom*
[4]*Jožef Stefan Institute, Jamova cesta 39, SI-1000 Ljubljana, Slovenia*
[5]*Faculty of Mathematics and Physics, University of Ljubljana, Jadranska ulica 19, SI-1000 Ljubljana, Slovenia*
[6]*PSI Center for Neutron and Muon Sciences CNM, 5232 Villigen PSI, Switzerland*

Centrosymmetric GdRu$_2$Si$_2$ exhibits a variety of multi-Q magnetic states as a function of temperature and applied magnetic field, including a square skyrmion-lattice phase. The material's behavior is strongly dependent on the direction of the applied field, with different phase diagrams resulting for fields applied parallel or perpendicular to the crystallographic c axis. Here, we present the results of muon-spin relaxation (μ^+SR) measurements on single crystals of GdRu$_2$Si$_2$. Our analysis is based on the computation of muon stopping sites and consideration of quantum zero-point motion effects of muons, allowing direct comparison with the underlying spin textures in the material. The muon site is confirmed experimentally, using angle-dependent measurements of the muon Knight shift. Using transverse-field μ^+SR with fields applied along either the [001] or [100] crystallographic directions, we distinguish between the magnetic phases in this system via their distinct muon response, providing additional evidence for the skyrmion and meron-lattice phases, while also suggesting the existence of RKKY-driven muon hyperfine coupling. Zero-field μ^+SR provides clear evidence for a transition between two distinct magnetically ordered phases at 39 K.

I. INTRODUCTION

Skyrmions are topologically protected vortices of magnetization that exist in some magnetically ordered materials [1]. The search for new materials that host a magnetic skyrmion state has been motivated by the numerous potential applications of skyrmions in the areas of ultraefficient information storage and spintronics [2]. Skyrmions are typically stabilized by the Dzyaloshinskii-Moriya interaction (DMI), which can only occur in systems that lack inversion symmetry. Magnets based on Gd (possessing $4f^7$ core states with $S = 7/2$, $L = 0$) are promising candidates for realizing noncollinear spin structures such as skyrmions, since the moments should show mostly nonpreferential orientation. Two Gd-based magnets where skyrmions have recently been discovered are Gd$_2$PdSi$_3$ [3] and Gd$_3$Ru$_4$Al$_{12}$ [4]. In these centrosymmetric materials, skyrmions have been proposed to be stabilized by either short- or long-range magnetic frustration rather than DMI. This can lead to interesting competition with other magnetic phases, and potentially new behavior of the skyrmion state. Skyrmions have also been observed in GdRu$_2$Si$_2$ [5], another centrosymmetric Gd-based magnet. However, the

structure of GdRu$_2$Si$_2$, shown in Fig. 1(a), comprises alternating square-lattice Gd and Ru$_2$Si$_2$ layers and therefore, unlike for Gd$_2$PdSi$_3$ and Gd$_3$Ru$_4$Al$_{12}$, short-range geometrical frustration cannot be used to explain the formation of the skyrmion lattice (SkL). Magnetic resonant x-ray scattering (RXS) and Lorentz transmission electron microscopy reveal the existence of a double-Q magnetic state, corresponding to a square SkL [5]. This is distinct from the hexagonal SkL found in Gd$_2$PdSi$_3$ and GdRu$_4$Al$_{12}$, and in the vast majority of the noncentrosymmetric skyrmion-hosting materials. Moreover, the existence of a square SkL has only been demonstrated [5] for applied fields $\boldsymbol{B}_0 \parallel$ [001], for which the SkL phase is stabilized at $B_0 \approx 2$ T. For fields in the ab plane, a different phase diagram is obtained [6,7]. The magnetic phase diagrams for $\boldsymbol{B}_0 \parallel$ [001] and $\boldsymbol{B}_0 \parallel$ [100] have been studied using RXS [7], with these measurements revealing a rich variety of double-Q magnetic structures, including the antiferroic order of meron/antimeron-like textures. Neutron diffraction measurements on single-crystal and polycrystalline ^{160}GdRu$_2$Si$_2$ found, in addition to scattering at the principal propagation vectors $\boldsymbol{q}_1$ and $\boldsymbol{q}_2$, higher-order satellites at $\boldsymbol{q}_1 + 2\boldsymbol{q}_2$. This prompted a revision of the zero-field magnetic ground state to a double-Q constant-moment magnetic structure, with one-dimensional topological charge density [8]. At small values of applied field, an additional phase has been identified just below T_N whose properties are less well understood, but which was recently revealed, in zero field, to involve a single magnetic propagation vector that splits
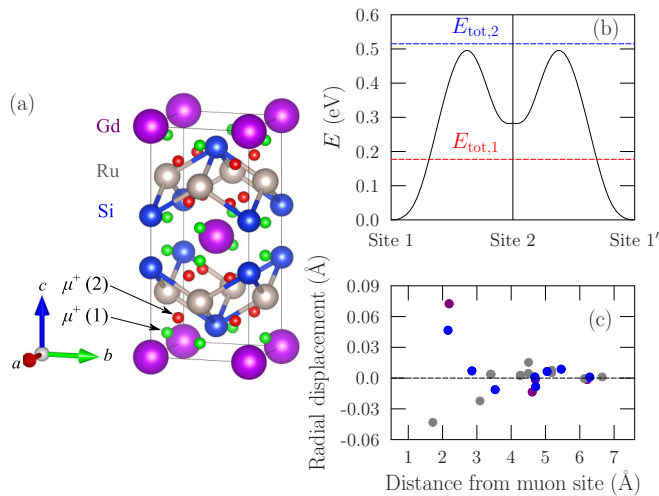
FIG. 1. (a) Two crystallographically distinct muon stopping sites in GdRu$_2$Si$_2$, obtained using DFT. (b) Energy barriers between muon sites. Red and blue lines indicate the total (classical plus quantum, zero-point) energy of the muon at sites 1 and 2, respectively. (c) Muon-induced displacements of atoms as a function of distance from the lowest-energy muon site.

into two wave vectors with different magnitudes upon further cooling [9].

Here, we use muon-spin spectroscopy (μ^+SR) [10] to probe the magnetic phases in GdRu$_2$Si$_2$ as a function of magnetic field and temperature. The μ^+SR technique has been shown to be sensitive to the distribution of magnetic fields arising from the SkL phase in Cu$_2$OSeO$_3$ [11], as well as those found in the helical [12] and conical [13] phases of skyrmion-hosting MnSi. Implanted muons have also been shown to effectively probe the emergent spin dynamics associated with Bloch SkL, such as in Cu$_2$OSeO$_3$ and Co$_x$Zn$_y$Mn$_{20-x-y}$ [14] and in Gd$_2$PdSi$_3$ [15], or those accompanying a Néel SkL, as found in GaV$_4$S$_8$ and GaV$_4$Se$_8$ [16,17]. Using transverse-field (TF) μ^+SR for magnetic fields applied along either the [001] or [100] direction, we show here how the response of the implanted muon reflects the occurrence of skyrmion and other double-Q magnetic phases in GdRu$_2$Si$_2$. Zero-field (ZF) μ^+SR measurements provide clear evidence for a transition between two distinct magnetically ordered phases at 39 K, showing that the phase reported just below $T_N = 45$ K is ordered throughout the bulk of the material. Our modeling, which includes muon-site determination and its confirmation via experiment, also provides an estimate of the low-temperature ordered moment of 4.8(1)μ_B and shows the influence of long-range Ruderman-Kittel-Kasuya-Yosida (RKKY) coupling in the system, via the muon's coupling to the electronic degrees of freedom.

The paper is structured as follows: in Sec. II we present the results of muon stopping site calculations using density functional theory (DFT), in Sec. III we present the results of μ^+SR measurements on GdRu$_2$Si$_2$ and discuss these with support from simulations of the magnetic field at the muon site for candidate magnetic structures, and finally we present our conclusions in Sec. IV. Additional details can be found in the Supplemental Material (SM) [18].

II. MUON SITE CALCULATIONS

Implanted muons are sensitive to the distribution of magnetic fields at the muon stopping sites. Knowledge of these sites can facilitate a quantitative understanding of μ^+SR measurements. Progress has recently been made in computing stopping sites using DFT [19], although treatment of quantum-mechanical effects such as zero-point motion has hitherto been limited to special cases [10,20]. We have used DFT methods to calculate the muon sites in GdRu$_2$Si$_2$ [18] and find two crystallographically distinct candidate sites [Fig. 1(a)]. These sites were further investigated to evaluate their stability. In the weakly bound adiabatic limit (i.e., with zero entanglement with nearby nuclear positions) [20], the zero-point energy of the muon can be approximated as the sum of the three highest-frequency phonon modes. The entanglement witness w_1, obtained by projecting the three highest-energy (normalized) phonon normal modes onto pure muon motion, summing the squared norms of the resulting (projected) phonon eigenvectors, and subtracting the upper bound 3 [20], can be used to determine whether the muon is in fact in this limit. This results in $w_1 = 0$ for zero muon-nuclear entanglement (weakly bound adiabatic limit) and $w_1 < 0$ in the entangled, many-body case. We obtained entanglement witnesses $w_1 = -0.0079$ and $w_1 = -0.0082$ for site 1 and site 2, respectively, which are both close to zero, confirming the validity of the weakly bound adiabatic approximation, i.e., the decoupling of muon vibrational modes from the vibrational modes of the lattice.

The energy barriers for moving a muon between sites 1 and 2 were calculated using transition state searches, and confirmed using the nudged elastic band method [21], yielding the energy profile in Fig. 1(b). However, on taking into account the quantum zero-point energy, a muon at site 2 (the higher-energy state of the two) has sufficient energy to overcome the energy barrier between its classical location and that of site 1. Site 2 is therefore not stable under quantum fluctuations of the muon position.

While the barrier from site 1 to site 2, and hence the barrier between adjacent instances of site 1 (i.e., site 1 and site 1'), is sufficiently high that we do not expect muons at site 1 to be able to leave this site classically, we also need to consider the possibility of quantum-mechanical tunneling. By considering the effective one-dimensional potential for the muon along the minimum-energy path between the classical turning points, i.e., where the black and red lines in Fig. 1(b) intersect, we used the WKB approximation to estimate a tunneling rate ≈ 0.05 Hz for muons to move between site 1 and site 1' [18], which corresponds to a significantly longer timescale than the one over which measurements are made. We therefore conclude that site 1 is the single crystallographically distinct stable stopping site in this material and we plot the displacements of the nearby atoms in the vicinity of this site in Fig. 1(c). The muon does not introduce any significant perturbations to its local environment, with all displacements <0.1 Å, and is therefore expected to be a faithful probe of the magnetism in this system. Note that these calculations do not take into account the possible effect of charge density waves, which have been proposed to result from the coupling between itinerant electrons and localized moments in this system [22], and could result in small perturbations to the muon site.
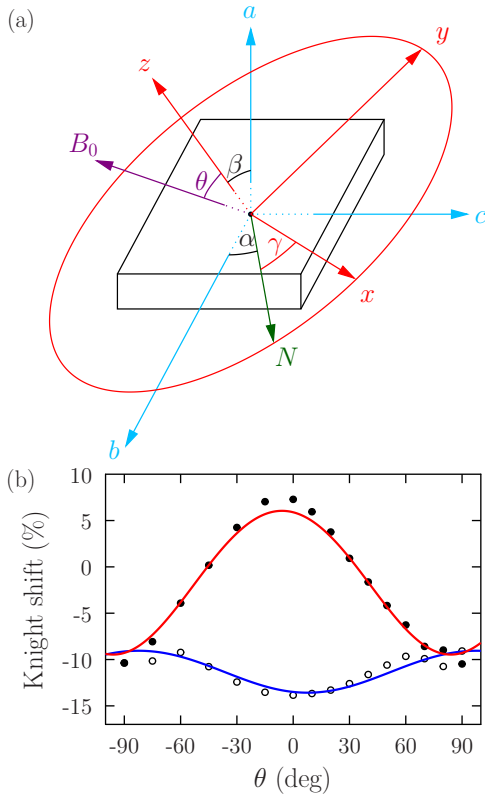
FIG. 2. (a) Schematic of the experimental geometry for the Knight shift measurements, indicating the direction of the applied magnetic field $\boldsymbol{B}_0$ in the crystallographic frame (a, b, c) of the sample. (b) Two components of the muon Knight shift as a function of the rotation angle θ.

III. RESULTS AND DISCUSSION

A. Angle-dependent Knight shift measurements

To further examine the muon site and its associated hyperfine coupling, we carried out angle-dependent measurements of the muon Knight shift on a single crystal of GdRu$_2$Si$_2$ with a large (100) face using the GPS spectrometer at the Swiss Muon Source, Paul Scherrer Institute (Switzerland). Measurements were made at 55 K, i.e., within the paramagnetic phase. The sample was enclosed in aluminum foil and attached to the end of a sample stick. These measurements were made in a spin-rotated configuration, with the initial muon-spin polarization making an angle $\approx 45°$ to the muon beam axis.

The experimental geometry is shown in Fig. 2(a). For the purpose of calculating the magnitude of the magnetic field at the muon site, we consider the crystallographic frame (a, b, c) of the sample to be fixed. We then define a second frame, the laboratory frame, such that the applied magnetic field $\boldsymbol{B}_0$, with magnitude 0.78 T, initially points along $\hat{\boldsymbol{z}}$ and rotates anticlockwise about $\hat{\boldsymbol{x}}$, with the angle of rotation denoted θ. The two coordinate systems are related by the Euler angles α, β, and γ, as shown in Fig. 2(a). Assuming perfect alignment of the crystal, i.e., $\alpha = \beta = \gamma = 0$, we have $\hat{\boldsymbol{z}} = \hat{\boldsymbol{a}}$ and $\hat{\boldsymbol{x}} = \hat{\boldsymbol{b}}$. This corresponds to the scenario in which the applied magnetic field is initially along [100] and the rotation axis of the sample stick is along [010]. The use of Euler angles allows us to capture any sample misalignment in our analysis.

At each rotation angle, we consider the components of the muon polarization measured in the four detectors perpendicular to the applied magnetic field: up, down, left, and right. These are all fitted to a function

$$A(t) = A_{\text{bg}} \cos(\omega_0 t + \phi) + \sum_{i=1}^{2} A_i e^{-\lambda_i t} \cos(\omega_i t + \phi), \quad (1)$$

where the first term is due to muons stopping outside the sample and precessing about the applied field, while the other two components correspond to muons stopping in the sample. The phase ϕ is allowed to vary for each detector, but is the same for all components in the fitting function, as would be expected for the magnetic field distribution arising from a field-polarized state. Note that it was not possible to separately resolve ω_1 and ω_2 for $\theta = -90°$ and hence these were fixed to be equal in the fitting procedure for this angle (as were λ_1 and λ_2).

For muons stopping at site 1 we would expect to observe two distinct components with frequencies shifted away from the Larmor frequency $\omega_0 = \gamma_\mu B_0$ corresponding to the applied field. For Gd moments pointing in a general direction within the ac plane, instances of site 1 lying on the a axis will experience a different dipolar magnetic field to those lying on the b axis. As each of the magnetically distinct instances of site 1 are expected to be occupied with equal probability, we fix $A_1 = A_2$ in Eq. (1). Furthermore, from a fit to the spectrum measured for $\theta = 0$, where the frequency shifts are at their largest, we find $(A_1 + A_2)/(A_1 + A_2 + A_{\text{bg}}) = 0.95(2)$. The ratio of the amplitudes is fixed at this value for fits at the other rotation angles. For each component, the precession frequency is related to the magnetic field at the muon site through $\omega_i = \gamma_\mu B_i$. Hence, we can compute the Knight shift at each of the muon sites through

$$K_i = \frac{\omega_i - \omega_0}{\omega_0}. \quad (2)$$

The muon Knight shifts corresponding to the two components of the asymmetry are shown as a function of direction of the applied magnetic field in Fig. 2(b). These two components exhibit the maximum separation for $\theta \approx 0$ and coincide when θ is close to $\pm 90°$. This can be understood in the case of perfect alignment of the crystal, for which a value of $\theta = 90°$ would correspond to the applied field, and hence the Gd moments, pointing along [00$\bar{1}$]. In that case, all instances of site 1 would become magnetically equivalent, and hence only a single Knight shift would be observed.

In this experiment, the contributions to the magnetic field at the muon site are as follows,

$$\boldsymbol{B}(\theta) = \boldsymbol{B}_0 + \boldsymbol{B}_{\text{dip}}(\theta) + \boldsymbol{B}_{\text{Lor}} + \boldsymbol{B}_{\text{cont}} + \boldsymbol{B}_{\text{demag}}(\theta), \quad (3)$$

where $\boldsymbol{B}_0$ is the applied magnetic field, $\boldsymbol{B}_{\text{dip}}(\theta)$ is the local dipolar field at the muon site, $\boldsymbol{B}_{\text{Lor}}$ is the Lorentz field, $\boldsymbol{B}_{\text{cont}}$ is the contact-hyperfine field, and $\boldsymbol{B}_{\text{demag}}(\theta)$ is the demagnetizing field. The Lorentz term $\boldsymbol{B}_{\text{Lor}}$ is proportional to the sample magnetization. We assume that the magnetic susceptibility is independent of field direction within the paramagnetic phase. Hence, we assume Gd moments with a magnitude μ_{Gd} in the direction of the applied field, where μ_{Gd} is allowed to vary in the fitting, but is assumed to have the same value for all

orientations of the applied field. Using this magnetic structure, we can calculate B_{Lor} and, using the dipolar tensor at the muon stopping site, the local dipolar field B_{dip} at each field angle.

The contact term B_{cont} was evaluated using the approach implemented in MuESR [23], whereby the hyperfine field is assumed to be isotropic and results from a scalar coupling to the magnetic moments. Each of the nearest-neighbor moments is assumed to contribute to the total hyperfine field by an amount inversely proportional to the cube of its distance from the muon. This field is then scaled by the hyperfine coupling constant A, leading to

$$B_{\text{cont}} = A \frac{2\mu_0}{3} \sum_{i=1}^{N} \frac{r_i^{-3}}{\sum_{j=1}^{N} r_j^{-3}} m_i, \tag{4}$$

where i (or j) denotes each of the N nearest-neighbor Gd atoms of the muon site ($N = 2$ in our case). Since all Gd moments are parallel to the applied magnetic field, this term results in a constant shift in both components of the Knight shift proportional to the hyperfine coupling A. Furthermore, since the two nearest-neighbor Gd atoms are equidistant from the muon site, they contribute equally to the hyperfine field in Eq. (4) and hence the scaling with distance is not important. The demagnetizing field

$$B_{\text{demag}} = -\mu_0 N M, \tag{5}$$

where the demagnetizing tensor N depends on the sample shape. For the sample used in this experiment N is not isotropic, and therefore the demagnetizing field exhibits an angular dependence.

We evaluated the demagnetizing tensor for our sample using an analytical solution obtained for rectangular prisms [24]. We approximated the sample as a rectangular plate with dimensions 5.7(4) mm by 4.36(2) mm, along b and c, respectively, and a thickness of 0.84(2) mm. (The greater uncertainty in the length of the crystal along the b axis reflects the fact that the crystal has two uncut rounded edges.) Averaging over the sample volume, this yields a diagonal demagnetizing tensor N with eigenvalues 0.717(2), 0.123(5), and 0.160(4).

The results of our fits to the muon Knight shift at the two muon sites are shown by the red and blue lines in Fig. 2(b) and show good agreement with the data. Best fits are obtained with $\alpha = -64(6)°$, $\beta = 17(2)°$, and $\gamma = 68(3)°$. This set of Euler angles results in an angle of $16°$ between the sample rotation axis and [010], while the angle between the initial magnetic field direction and [100] is given by $\beta = 17(2)°$. Such a degree of misalignment is very plausible, given the experimental setup. The fitting yields a value $A = -0.0094(4)$ Å^{-3} for the hyperfine coupling constant. The fitted Gd moment is $\mu_{\text{Gd}} = 0.46(2)\mu_B$. Magnetometry measurements [18] made on this sample at 0.5 T give a moment of $\mu_{\text{Gd}} = 0.437(15)\mu_B$ at 55 K. Assuming that the susceptibility is independent of field at this temperature would give a moment $\mu_{\text{Gd}} = 0.68(2)\mu_B$ at 0.78 T, which is larger than the moment suggested by this analysis.

In summary, the results of these measurements are consistent with muons stopping in GdRu$_2$Si$_2$ at a single crystallographically distinct site. The observation of two distinct muon Knight shifts rules out alternative sites with axial symmetry, such as the site at (0.5, 0.5, 0) that has been proposed

for the isostructural compound CeRu$_2$Si$_2$ [25], which corresponds to a single magnetically distinct site for all moment directions. As seen in Fig. 2(b), a good fit can be made to the data by assuming that site 1 is the muon stopping site. These measurements therefore provide experimental confirmation for the muon site that we calculated using DFT, and which serves as the basis for much of the analysis in the rest of this paper. They also indicate the presence of a significant negative hyperfine field at the muon site, which will be important when considering the magnetic field at the muon site measured for other phases in GdRu$_2$Si$_2$. Negative hyperfine coupling constants of -0.45 and -0.518 T μ_B^{-1} were found for the paramagnetic phases of MnGe [26] and MnSi [27], respectively. These are significantly larger than the value found here for GdRu$_2$Si$_2$, which in these units is $A = -0.073(3)$ T μ_B^{-1}, but give rise to similar hyperfine fields once the larger size of the Gd moments is taken into account.

B. Transverse-field μ^+SR measurements

Transverse-field μ^+SR measurements were made on aligned crystals of GdRu$_2$Si$_2$ using the HAL-9500 spectrometer at the Swiss Muon Source. In these measurements, the muon spin precesses about the sum of the external magnetic field, which is oriented perpendicular to the initial muon-spin direction, and any internal magnetic fields present in the sample. Two sets of measurements were made: one with the crystals oriented such that applied field B_0 pointed along [001] and another set with the crystals oriented such that B_0 pointed along the [100] direction. Spectra were measured after zero-field cooling the sample.

We first consider the spectra measured at $T = 40$ K, where we can access the field-polarized state. Fourier transform (FT) μ^+SR spectra measured at different fields are shown in Fig. 3 for each of the orientations. For $B_0 \parallel$ [001] the spectra comprise a peak close to the applied field and a secondary peak at lower fields which becomes more prominent as the applied field is increased. (We note that the central peak is split in two for all of the TF spectra measured on this material, which could result from a fraction of the muons stopping in parts of the sample where the internal field almost, but not completely, cancels, such as domain walls or surfaces.) For $B_0 \parallel$ [100] there is an additional peak at fields larger than B_0 that is absent for the other orientation. We therefore fit the spectra for fields along [001] and [100] to the sum of two or three Lorentzians, respectively, and plot the behavior of the peak centers in Figs. 3(d) and 3(h), respectively. We see that the magnitude of the field shifts at the two peaks initially increases approximately linearly with the applied field, but then begins to level off, suggesting that the magnetization is starting to saturate. We also note the absence of any satellite peaks for $B_0 = 0.5$ T $\parallel$ [001] in Fig. 3(a), with the magnetic phase diagram for this orientation [shown in Fig. 4(i)] having a phase boundary between 0.5 and 1 T at this temperature. This suggests that the low-field, higher-temperature magnetically ordered state gives rise to a broad distribution of magnetic fields at the muon site, relaxing the contribution of muons stopping in the sample out of the TF spectra, a scenario which is consistent with our ZF spectra, discussed in Sec. III C, which show a large relaxation rate at this temperature. On the other hand, spectra measured
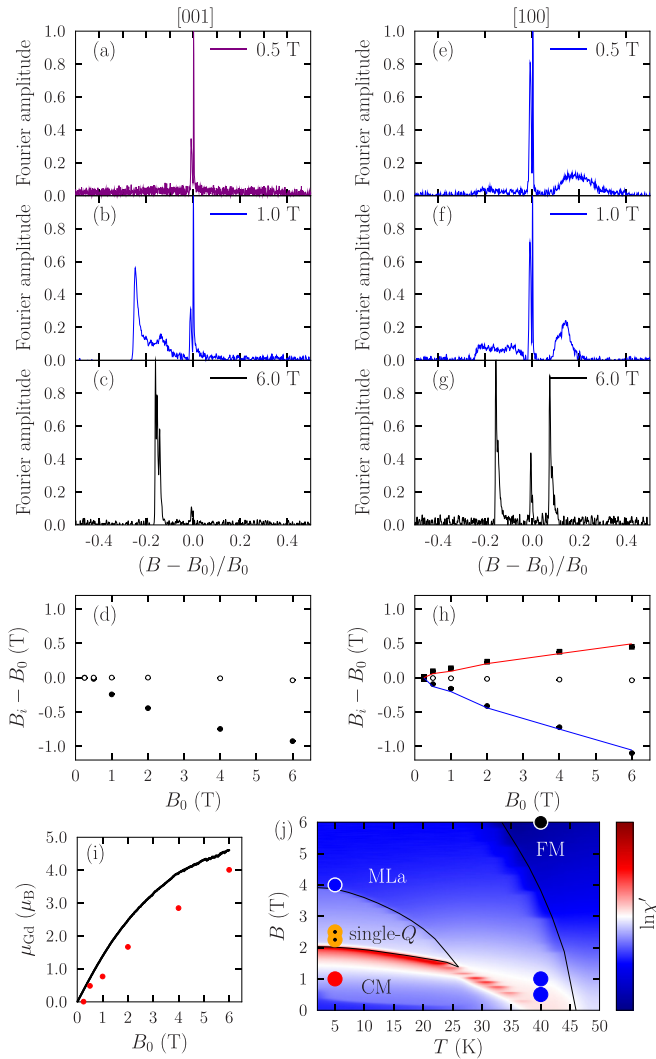
FIG. 3. Fourier transform TF μ^+SR spectra measured at $T = 40$ K for applied magnetic fields along (a)–(c) [001] and (e)–(g) [100]. Positions of peaks as a function of applied field B_0 along [001] and [100] are shown in (d) and (h), respectively. Red and blue lines in (h) correspond to fits of the internal field at muon sites lying on the a axis or b axis, respectively, as a function of the extracted Gd magnetic moment. (i) Magnetic moment of the Gd ions at 40 K, obtained from the separation of the peaks in the muon spectra (red circles) and magnetometry (black). (j) Real part of the ac susceptibility as a function of temperature and magnetic field for applied magnetic fields along [100]. Circles on the phase diagram correspond to the FT μ^+SR spectra presented in this paper, with colors corresponding to the lines used to plot the spectra.

FIG. 4. Fourier transform TF μ^+SR spectra measured at $T = 5$ K for applied magnetic fields along (a)–(d) [001] and (e)–(h) [100]. Black lines indicate simulations of the spectra. (i) Magnetic phase diagram for applied fields along [001], using phase boundaries obtained in Ref. [5].

at 0.5 and 1.0 T for $\boldsymbol{B}_0 \parallel$ [100], shown in Figs. 3(e) and 3(f), respectively, are expected to occupy the same magnetic phase [as seen in our ac susceptibility measurements shown in Fig. 3(j)] and both show satellite peaks. This suggests the zero-field ordered state survives up to higher fields applied along [001] than for those along [100].

The number of peaks observed for each of the field orientations reflects the symmetry of the muon stopping site. The local magnetic field at the muon site is the sum of the externally applied field and dipolar, Lorentz, demagnetizing,
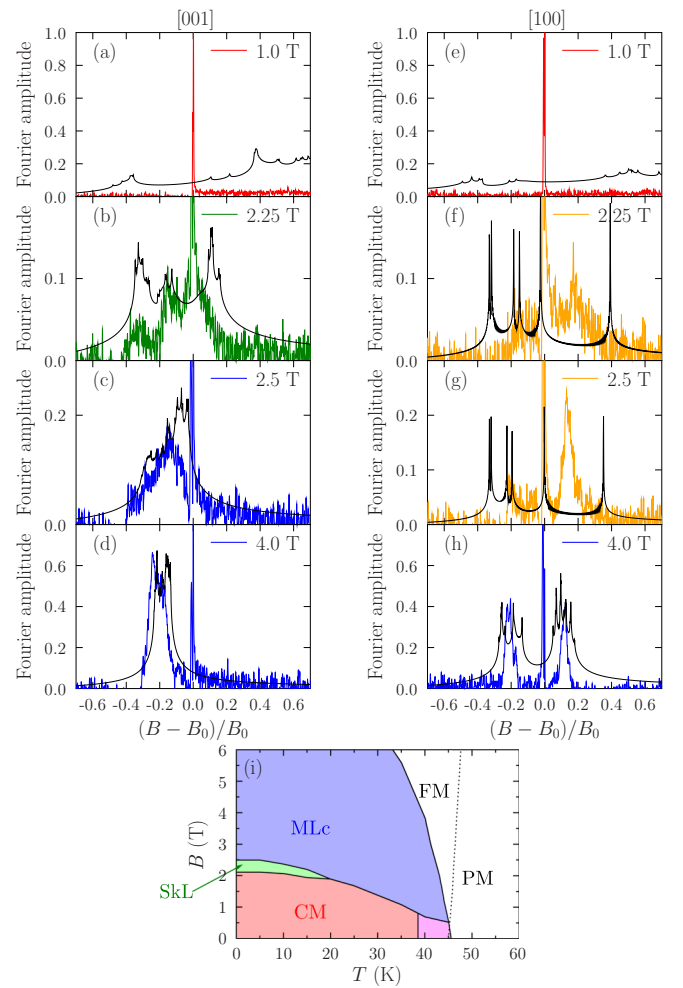
and hyperfine fields. For Gd moments along c, muons at site 1 will all experience an internal field of $(-0.063 - 0.140N + 7.77A)\mu_{Gd}$ T along c, where the first term is sum of the dipolar and Lorentz fields, the second term is the demagnetizing field, with the demagnetizing factor N depending on the sample shape, and the final term is the hyperfine field, which is proportional to the hyperfine coupling constant A, measured in Å^{-3}. All of these contributions to the internal field are proportional to the Gd magnetic moment μ_{Gd}, which in this expression is measured in Bohr magnetons. On the other hand, for moments along a, instances of site 1 lying on the a axis will experience a field $(0.295 - 0.140N + 7.77A)\mu_{Gd}$ T along a, whereas the crystallographically equivalent site lying on the b axis will instead experience a field $(-0.091 - 0.140N + 7.77A)\mu_{Gd}$ T. For $\boldsymbol{B}_0 \parallel$ [100] the separation of the satellite peaks, ΔB, is therefore related to μ_{Gd} by $\Delta B = 0.386\mu_{Gd}$ T. The development of μ_{Gd} as a function of applied magnetic field is shown in Fig. 3(i). We have also measured the Gd moment as a function of magnetic field using magnetometry [18] [Fig. 3(i)]. The values of μ_{Gd} obtained using these approaches

show reasonable agreement, though we note that those obtained from magnetometry are consistently larger and have a slightly different functional dependence with applied field. Taking the sample geometry to be a flat plate with a perpendicular magnetization, we assume $N \approx 1$. (We note the larger sample area obtained for this mosaic of crystals, compared to a single crystal, means that we expect the out-of-plane component of the demagnetizing tensor to be closer to 1 than was the case for the sample used in our angle-dependent Knight shift measurements.) Fitting either the positive or negative field shifts for $B_0 \parallel [100]$ to a straight line in $\mu_{Gd}(B_0)$ [red or blue lines in Fig. 3(h), respectively] yields $A = -0.0040(9)$ Å^{-3}, which is similar to the hyperfine coupling obtained from our analysis of angle-dependent muon Knight shift measurements. This negative hyperfine contribution can be explained by the spin-polarization of conduction electrons through the RKKY interaction, which has been predicted to play an important role in stabilizing the skyrmion lattice in GdRu$_2$Si$_2$ [28]. The multiplicity of the peaks for fields along [100] is consistent with our calculated muon site and with our TF measurements made in the paramagnetic phase at 55 K.

We now turn to the spectra measured at $T = 5$ K, where several distinct magnetic structures exist as a function of applied magnetic field [5,7]. FT μ^+SR spectra are shown in Fig. 4 for each orientation. For $B_0 < 2.25$ T, the spectra comprise a split peak, close to the applied field [Figs. 4(a) and 4(e)]. For higher fields $B_0 \parallel [001]$ [Figs. 4(b)–4(d)], the spectra contain additional spectral weight at fields below the applied field, whereas for $B_0 \parallel [100]$ [Figs. 4(f)–4(h)], we see a pair of satellite peaks, above and below B_0. As before, this reflects the symmetry of the muon site for each field orientation. However, the features in the spectra are much broader for $T = 5$ K, suggesting that the system adopts magnetic structures that give rise to a wider distribution of fields. These become sharper at higher applied fields, as the field-polarized component of the magnetic structure becomes more significant.

Knowledge of the muon stopping site and the candidate magnetic structures allows us to simulate the expected μ^+SR spectra [18]. Simulated spectra for $T = 5$ K are shown alongside the data in Figs. 4(a)–4(h). (Since the sharp peak at the applied field is due to muon stopping in the silver sample holder, this does not appear in our simulations.) As seen in Fig. 3(i), the Gd moment measured using μ^+SR is consistently smaller than the $7.0\mu_B$ expected for an isolated Gd^{3+} ion, in contrast to the results of two neutron diffraction studies [8,9], which have shown that the size of the ordered moment is broadly consistent with $7.0\mu_B$. For our simulations, we take $\mu_{Gd} = 4.8(1)\mu_B$, deduced from zero-field μ^+SR at low temperatures presented in Sec. III C, where possible reasons for this discrepancy are also discussed.

For the spectra measured at $B_0 = 1.0$ T [Figs. 4(a) and 4(e)], we see only a sharp peak at the applied magnetic feature, with no other notable features. This peak is due to muons stopping outside of the sample, suggesting that muons stopping inside the sample experience a broad distribution of magnetic fields and therefore have their contribution to the TF spectra dephased. This is consistent with our simulations based on the constant-moment magnetic structure proposed in Ref. [8] [denoted CM in Fig. 4(i)], which leads to a Fourier spectrum

with weight spread across a wide frequency window with no notable peaks. The simulated spectrum for $B_0 \parallel [001]$ does, however, predict some additional spectral weight at fields around 0.5 T above the applied field, which is not seen in experiment, although the overall broadness of the spectrum means that this would likely be difficult to resolve in practice.

We first focus on the spectra measured for $B_0 \parallel [001]$. For $B_0 = 2.25$ T, GdRu$_2$Si$_2$ has been proposed to host a square SkL phase [5]. The corresponding μ^+SR spectrum in Fig. 4(b) exhibits two peaks at fields below the applied field, whose locations show good agreement with those simulated for an approximate realization of a square SkL. Our simulation also predicts a peak just above the applied field, suggesting that a fraction of the implanted muons will be at sites where the internal field is well aligned with the external field. Due to the anisotropic nature of the dipolar tensor at the muon site, a magnetic structure with moments polarized along the c axis results in a dipolar field that points in the opposite direction to the magnetization, and hence the external field, as seen in Fig. 3(c). This therefore highlights the role of the incommensurate components of the magnetic moments in giving rise to a local field at the muon site aligned with the externally applied field. However, we note that this high-field feature is not resolved in the measured spectrum, possibly due to being too close to the central peak.

The 2.25 T spectrum is qualitatively different from those measured at 2.5 [Fig. 4(c)] and 4 T [Fig. 4(d)] for this orientation, allowing us to clearly distinguish the response of the muon to the SkL from that arising from the other multi-Q magnetic structures that are realized in this system. For the higher fields along [001], this has been proposed to be the checkerboard antiferroic order of meron/antimeron-like textures (MLc) [7]. The $B_0 \geqslant 2.5$ T spectra both comprise a satellite peak below the applied field, although the shape of the satellite is distinct in each case. Our simulated spectra based on the MLc magnetic structure show fair agreement with experiment for both values of B_0. The difference between the spectra measured at 2.25 [Fig. 4(b)] and 2.5 T [Fig. 4(c)] can be explained by the fact that the helical components of the SkL magnetic structure rotate into and out of the c-axis direction, either aligning or antialigning with the ferromagnetic component, whereas the modulated parts of the moment in the MLc phase remain within the ab plane (and therefore perpendicular to the ferromagnetic component). Thus the former magnetic structure more effectively splits the spectral weight into distinct peaks, whereas the latter only results in broadening of the low-field feature.

Turning to the spectra measured for $B_0 \parallel [100]$, we note that, in contrast to $B_0 \parallel [001]$, applied fields with magnitudes $B_0 = 2.25$ T and $B_0 = 2.5$ T in this orientation are expected to result in a single-Q conical magnetic structure. The spectra measured in this phase [Figs. 4(f) and 4(g)] comprise pairs of satellite peaks, one above B_0 and one below. These features are fairly broad and somewhat difficult to resolve in experiment for $B_0 = 2.25$ T, but become sharper at $B_0 = 2.5$ T. Our simulated spectra can be interpreted as a pair of shifted Overhauser distributions [27] resulting from a helical magnetic structure propagating along the a axis, which leads to different magnetic fields for muons sitting along the a axis from those lying on the b axis. An additional ferromagnetic

component shifts the centers of these distributions, such that one is centered on a field above B_0 and one on a field below, and also results in a small splitting of the peaks within this distribution, which is particularly noticeable for the distribution at fields below B_0. It is difficult to reconcile these spectra with those observed in experiment. The peaks observed in the experimental spectra suggest the presence of a significant field-polarized ferromagnetic component, which was included in the magnetic structure used in our simulations, but these are broadened, rather than experiencing the splitting that our simulations predict. We therefore suggest that these spectra are incompatible with the proposed single-Q magnetic structure. It is possible that the magnetic structure for this phase needs to be revised, and further work on this phase would be instructive.

At $B_0 = 4$ T, an applied field parallel to [100] gives rise to another checkerboard phase, where the modulations in magnetic moment are rotated relative to those for $\boldsymbol{B}_0 \parallel [001]$, in order to remain perpendicular to the applied field [7]. For both field orientations, the magnetic structures at $B_0 = 4$ T contain substantial field-polarized components, so the locations and multiplicity of the peaks mostly reflect the symmetry of the muon sites, as was discussed for the spectra measured at $T = 40$ K.

C. Zero-field μ^+SR measurements

Zero-field μ^+SR measurements were made on two aligned GdRu$_2$Si$_2$ single crystals using the GPS spectrometer. The ZF μ^+SR spectra exhibit a very quickly relaxing oscillating asymmetry. The first 0.1 μs of the spectra were fitted to the function

$$A(t) = A_1 \exp(-\lambda_1 t) \cos(2\pi f t + \phi) + A_2 \exp(-\lambda_2 t), \quad (6)$$

where the oscillating and nonoscillating components of the asymmetry have amplitudes A_1 and A_2 and relaxation rates λ_1 and λ_2, respectively. The amplitudes A_1 and A_2 and the phase ϕ were globally refined, with values $A_1 = 12.6(3)\%$, $A_2 = 5.56(4)\%$, and $\phi = -17(2)°$. The temperature dependence of the variable parameters is shown in Fig. 5. The muon precession frequency f serves as a magnetic order parameter for the system and exhibits a discontinuity in its derivative that suggests a transition between two distinct magnetic phases, both ordered throughout the bulk. The frequencies $f(T)$ were fitted to

$$f(T) = \begin{cases} f_1[1 - (T/T_c)^\alpha]^{\beta_1} & \text{for } 0 \leqslant T \leqslant T_{N1}, \\ f_2(1 - T/T_{N2})^{\beta_2} & \text{for } T_{N1} \leqslant T \leqslant T_{N2}, \end{cases} \quad (7)$$

where $f_2 = f_1 \frac{[1-(T_{N1}/T_c)^\alpha]^{\beta_1}}{(1-T_{N1}/T_{N2})^{\beta_2}}$, ensuring that $f(T)$ is continuous at $T = T_{N1}$. This fitting yields $f_1 = 129(3)$ MHz, $\alpha = 4.06(8)$, $\beta_1 = 0.49(8)$, $\beta_2 = 0.36(2)$, $T_c = 39.5(1)$ K, and transition temperatures $T_{N1} = 38.8(1)$ K and $T_{N2} = 44.95(1)$ K. The critical exponent $\beta_2 = 0.36(2)$ for the transitions between the higher-temperature ordered phase and the paramagnetic phase shows good agreement with the value $\beta = 0.366$ expected for a 3D Heisenberg magnet [29]. The transition at T_{N1} can also be seen in the relaxation rates, with λ_1 [Fig. 5(f)] and λ_2 [Fig. 5(g)] exhibiting discontinuous increases and decreases, respectively.
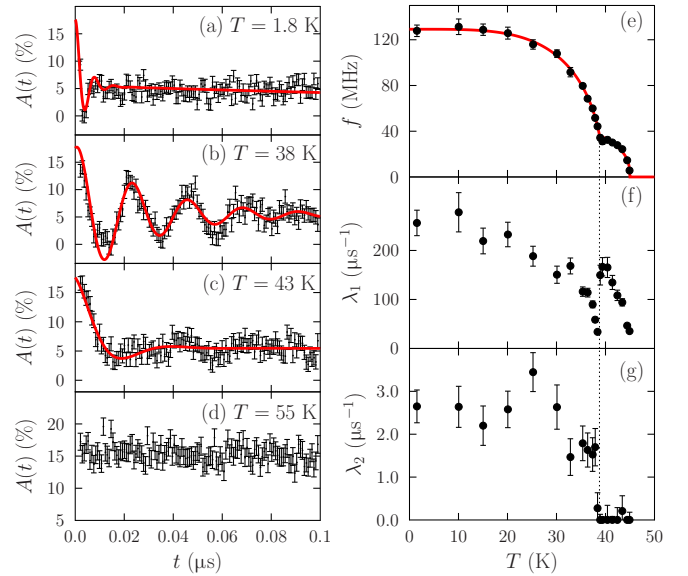

FIG. 5. Zero-field μ^+SR spectra measured at (a) 1.8 K, (b) 38 K, (c) 43 K, and (d) 55 K. Temperature dependence of (e) the muon procession frequency f and the relaxation rates (f) λ_1 and (g) λ_2 in Eq. (6).

We have simulated the ZF μ^+SR data across the temperature range, using candidate magnetic structures proposed in other studies [8,9]. We have modeled the data for $T < T_{N1}$ using the double-Q constant-moment (CM) magnetic structure with topological charge stripes proposed in Ref. [8]. Fitting the simulated spectra to the data provides the T dependence of the Gd magnetic moment μ_{Gd}. Furthermore, the effect of dynamics has been incorporated in these simulations using the strong collision approximation, thereby providing an estimate for the characteristic rate ν of spin fluctuations. Fits at representative temperatures, as well as the temperature dependence of these parameters, are shown in Fig. 6. We find an ordered
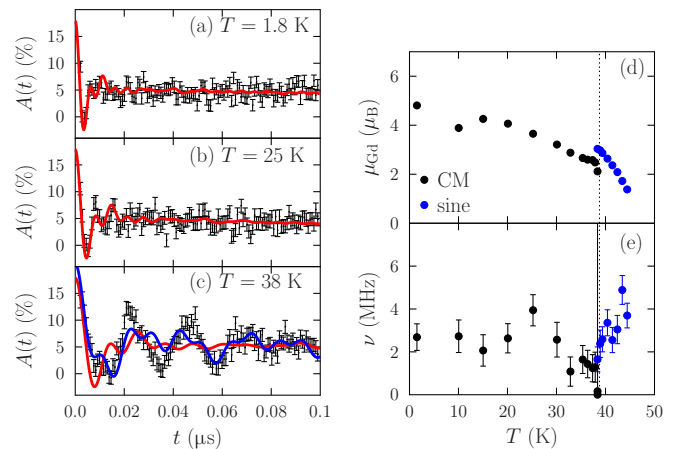

FIG. 6. Fits to a model based on the constant-moment solution for data measured at (a) 1.8 K, (b) 25 K, and (c) 38 K. The blue line in (c) indicates a fit to an alternative model based on a sine magnetic structure. (d) Gd magnetic moments and (e) fluctuation rates ν extracted using simulations of the μ^+SR spectra as a function of temperature.

moment of $4.8(1)\mu_B$ at $T = 1.5$ K, which is $\approx 30\%$ smaller than the full ionic value of $7.0\mu_B$. The Gd moment is obtained from the scale factor relating the simulated magnetic fields at the muon site to those observed in experiment, and hence this discrepancy could result from contributions to the magnetic field that are not accounted for by our model, such as those from the itinerant electrons.

The extracted fluctuation rates $\nu \approx 3$ MHz are significantly smaller than the relaxation rates λ_1 that accompany the relaxing part of the asymmetry, indicating that this relaxation is mostly due to the distribution of static magnetic fields resulting from the incommensurate magnetic structure. They are also much smaller than the precession frequency f, implying we are in a slowly fluctuating regime (assuming the fluctuating amplitude is of a similar order of magnitude to the static field). The discontinuous behavior of λ_1 at T_{N1} is therefore evidence for a significant change in the magnetic structure at this temperature. The fluctuation rates ν obtained from our simulations are similar in magnitude to the slow relaxation rate λ_2, consistent with the interpretation that this relaxation is due to dynamics flipping the muon spin at sites where the local magnetic field is parallel to the muon spin, in the slow fluctuation limit. We note that the relative magnitudes of A_1 and A_2 are consistent with those of the oscillating and nonoscillating parts, respectively, of the polarization function obtained by our model.

Unlike the magnetic ground state [8], the higher-temperature magnetically ordered phase has not been unambiguously identified. However, a recent powder neutron powder diffraction study [9] proposed three candidate single-Q magnetic structures for this phase, with those measurements being unable to distinguish between them. We therefore simulated μ^+SR spectra based on each of the models and fitted these to our data measured at $T \geqslant 38$ K. All of these models provided similar quality fits to the data, with a so-called sine magnetic structure with moments along the [011] direction being the best, and also being the only model that gives a magnetic moment that decreases monotonically with increasing temperature, as shown in Fig. 6(d). (We note that for these sine magnetic structures, which do not have a constant magnetic moment amplitude, μ_{Gd} represents the maximum value of the magnetic moment.) This magnetic structure also provides a better fit to the spectrum measured at $T = 38$ K than the constant-moment solution, as indicated by the blue line in Fig. 6(c). Our modeling also indicates that the fluctuation rate increases with increasing temperature on approaching T_{N2}, as shown in Fig. 6(e), but remains within the slow fluctuation limit. This suggests that the distribution of static magnetic fields resulting from an incommensurate magnetic structure is also responsible for the majority of the relaxation observed in this higher-temperature ordered phase.

IV. CONCLUSION

We have illustrated how implanted muons are sensitive to the magnetic phases in GdRu$_2$Si$_2$, providing evidence for skyrmion and meron-lattice magnetic phases. In contrast, μ^+SR spectra measured for intermediate fields along [100] are inconsistent with the previously proposed single-Q magnetic structure, suggesting that this phase needs to be revised. We demonstrate a significant, negative hyperfine contribution to the local magnetic field at the muon site, due to conduction electrons becoming spin polarized through the RKKY interaction. This significant hyperfine field is also observed in our angle-dependent measurements of the muon Knight shift, which also provide strong experimental evidence for the muon stopping sites that form the basis of much of our analysis. Zero-field measurements as a function of temperature demonstrate a transition between two distinct bulk magnetically ordered states at $T_{N1} = 38.8(1)$ K.

DATA AVAILABILITY

Data presented in this paper are available [30].

[1] T. Lancaster, Skyrmions in magnetic materials, Contemp. Phys. **60**, 246 (2019).

[2] A. Fert, N. Reyren, and V. Cros, Magnetic skyrmions: Advances in physics and potential applications, Nat. Rev. Mater. **2**, 17031 (2017).

[3] T. Kurumaji, T. Nakajima, M. Hirschberger, A. Kikkawa, Y. Yamasaki, H. Sagayama, H. Nakao, Y. Taguchi, T.-H. Arima, and Y. Tokura, Skyrmion lattice with a giant topological Hall effect in a frustrated triangular-lattice magnet, Science **365**, 914 (2019).

[4] M. Hirschberger, T. Nakajima, S. Gao, L. Peng, A. Kikkawa, T. Kurumaji, M. Kriener, Y. Yamasaki, H. Sagayama, H. Nakao, K. Ohishi, K. Kakurai, Y. Taguchi, X. Yu, T.-H. Arima, and Y. Tokura, Skyrmion phase and competing magnetic orders on a breathing kagomé lattice, Nat. Commun. **10**, 5831 (2019).

[5] N. D. Khanh, T. Nakajima, X. Yu, S. Gao, K. Shibata, M. Hirschberger, Y. Yamasaki, H. Sagayama, H. Nakao, L. Peng, K. Nakajima, R. Takagi, T.-H. Arima, Y. Tokura, and S. Seki, Nanometric square skyrmion lattice in a centrosymmetric tetragonal magnet, Nat. Nanotechnol. **15**, 444 (2020).

[6] A. Garnier, D. Gignoux, D. Schmitt, and T. Shigeoka, Giant magnetic anisotropy in tetragonal GdRu$_2$Ge$_2$ and GdRu$_2$Si$_2$, Phys. B: Condens. Matter **222**, 80 (1996).

[7] N. D. Khanh, T. Nakajima, S. Hayami, S. Gao, Y. Yamasaki, H. Sagayama, H. Nakao, R. Takagi, Y. Motome, Y. Tokura, T.-h. Arima, and S. Seki, Zoology of multiple-Q spin textures in a centrosymmetric tetragonal magnet with itinerant electrons, Adv. Sci. **9**, 2105452 (2022).

[8] G. D. A. Wood, D. D. Khalyavin, D. A. Mayoh, J. Bouaziz, A. E. Hall, S. J. R. Holt, F. Orlandi, P. Manuel, S. Blügel, J. B. Staunton, O. A. Petrenko, M. R. Lees, and G. Balakrishnan, Double-Q ground state with topological charge stripes in the centrosymmetric skyrmion candidate GdRu$_2$Si$_2$, Phys. Rev. B **107**, L180402 (2023).

[9] J. A. M. Paddison, J. Bouaziz, A. F. May, Q. Zhang, S. Calder, D. Abernathy, J. B. Staunton, S. Blügel, and A. D. Christianson, Spin dynamics of the centrosymmetric skyrmion material GdRu$_2$Si$_2$, Cell Rep. Phys. Sci. **5**, 102280 (2024).

[10] S. J. Blundell, R. De Renzi, T. Lancaster, and F. L. Pratt, *Muon Spectroscopy: An Introduction* (Oxford University Press, 2021).

[11] T. Lancaster, R. C. Williams, I. O. Thomas, F. Xiao, F. L. Pratt, S. J. Blundell, J. C. Loudon, T. Hesjedal, S. J. Clark, P. D. Hatton, M. Ciomaga Hatnean, D. S. Keeble, and G. Balakrishnan, Transverse field muon-spin rotation signature of the skyrmion-lattice phase in Cu$_2$OSeO$_3$, Phys. Rev. B **91**, 224408 (2015).

[12] P. Dalmas de Réotier, A. Maisuradze, A. Yaouanc, B. Roessli, A. Amato, D. Andreica, and G. Lapertot, Determination of the zero-field magnetic structure of the helimagnet MnSi at low temperature, Phys. Rev. B **93**, 144419 (2016).

[13] P. Dalmas de Réotier, A. Maisuradze, A. Yaouanc, B. Roessli, A. Amato, D. Andreica, and G. Lapertot, Unconventional magnetic order in the conical state of MnSi, Phys. Rev. B **95**, 180403(R) (2017).

[14] T. J. Hicken, M. N. Wilson, K. J. A. Franke, B. M. Huddart, Z. Hawkhead, M. Gomilšek, S. J. Clark, F. L. Pratt, A. Štefančič, A. E. Hall, M. Ciomaga Hatnean, G. Balakrishnan, and T. Lancaster, Megahertz dynamics in skyrmion systems probed with muon-spin relaxation, Phys. Rev. B **103**, 024428 (2021).

[15] M. Gomilšek, T. J. Hicken, M. N. Wilson, K. J. A. Franke, B. M. Huddart, A. Štefančič, S. J. R. Holt, G. Balakrishnan, D. A. Mayoh, M. T. Birch *et al.*, Anisotropic skyrmion and multi-q spin dynamics in centrosymmetric Gd$_2$PdSi$_3$, Phys. Rev. Lett. **134**, 046702 (2025).

[16] K. J. A. Franke, B. M. Huddart, T. J. Hicken, F. Xiao, S. J. Blundell, F. L. Pratt, M. Crisanti, J. A. T. Barker, S. J. Clark, A. Štefančič, M. C. Hatnean, G. Balakrishnan, and T. Lancaster, Magnetic phases of skyrmion-hosting GaV$_4$S$_{8-y}$Se$_y$ ($y = 0, 2, 4, 8$) probed with muon spectroscopy, Phys. Rev. B **98**, 054428 (2018).

[17] T. J. Hicken, S. J. R. Holt, K. J. A. Franke, Z. Hawkhead, A. Štefančič, M. N. Wilson, M. Gomilšek, B. M. Huddart, S. J. Clark, M. R. Lees, F. L. Pratt, S. J. Blundell, G. Balakrishnan, and T. Lancaster, Magnetism and Néel skyrmion dynamics in GaV$_4$S$_{8-y}$Se$_y$, Phys. Rev. Res. **2**, 032001(R) (2020).

[18] See Supplemental Material at http://link.aps.org/supplemental/10.1103/PhysRevB.111.054440 for further details of the density functional theory calculations and simulations of the magnetic field distributions and which includes Refs. [31–45].

[19] S. J. Blundell and T. Lancaster, DFT + μ: Density functional theory for muon site determination, Appl. Phys. Rev. **10**, 021316 (2023).

[20] M. Gomilšek, F. L. Pratt, S. P. Cottrell, S. J. Clark, and T. Lancaster, Many-body quantum muon effects and quadrupolar coupling in solids, Commun. Phys. **6**, 142 (2023).

[21] G. Henkelman and H. Jonsson, Improved tangent estimate in the nudged elastic band method for finding minimum energy paths and saddle points, J. Chem. Phys. **113**, 9978 (2000).

[22] Y. Yasui, C. J. Butler, N. D. Khanh, S. Hayami, T. Nomoto, T. Hanaguri, Y. Motome, R. Arita, T.-H. Arima, Y. Tokura, and S. Seki, Imaging the coupling between itinerant electrons and localised moments in the centrosymmetric skyrmion magnet GdRu$_2$Si$_2$, Nat. Commun. **11**, 5925 (2020).

[23] P. Bonfà, I. J. Onuorah, and R. D. Renzi, Introduction and a quick look at MUESR, the magnetic structure and mUon embedding site refinement suite, JPS Conf. Proc. **21**, 11052 (2018).

[24] R. I. Joseph and E. Schlömann, Demagnetizing field in nonellipsoidal bodies, J. Appl. Phys. **36**, 1579 (1965).

[25] A. Amato, R. Feyerherm, F. N. Gygax, and A. Schenck, μ^+-site in heavy-fermion compounds, Hyperfine Interact. **104**, 115 (1997).

[26] N. Martin, M. Deutsch, F. Bert, D. Andreica, A. Amato, P. Bonfà, R. De Renzi, U. K. Rößler, P. Bonville, L. N. Fomicheva, A. V. Tsvyashchenko, and I. Mirebeau, Magnetic ground state and spin fluctuations in MnGe chiral magnet as studied by mUon spin rotation, Phys. Rev. B **93**, 174405 (2016).

[27] A. Amato, P. Dalmas de Réotier, D. Andreica, A. Yaouanc, A. Suter, G. Lapertot, I. M. Pop, E. Morenzoni, P. Bonfà, F. Bernardini, and R. De Renzi, Understanding the μSR spectra of MnSi without magnetic polarons, Phys. Rev. B **89**, 184425 (2014).

[28] J. Bouaziz, E. Mendive-Tapia, S. Blügel, and J. B. Staunton, Fermi-surface origin of skyrmion lattices in centrosymmetric rare-earth intermetallics, Phys. Rev. Lett. **128**, 157206 (2022).

[29] S. J. Blundell, *Magnetism in Condensed Matter* (Oxford University Press, Oxford, 2000).

[30] B. M. Huddart, A. Hernández-Melián, G. D. A. Wood, D. A. Mayoh, M. Gomilšek, Z. Guguchia, C. Wang, T. J. Hicken, S. J. Blundell, G. Balakrishnan, and T. Lancaster, 2025, https://doi.org/10.15128/r15138jd91z.

[31] R. S. Hayano, Y. J. Uemura, J. Imazato, N. Nishida, T. Yamazaki, and R. Kubo, Zero- and low-field spin relaxation studied by positive muons, Phys. Rev. B **20**, 850 (1979).

[32] F. Pratt, WIMDA: A muon data analysis program for the Windows PC, Phys. B: Condens. Matter **289–290**, 710 (2000).

[33] F. James and M. Roos, Minuit—a system for function minimization and analysis of the parameter errors and correlations, Comput. Phys. Commun. **10**, 343 (1975).

[34] H. Dembinski, P. Ongmongkolkul, C. Deil, H. Schreiner, M. Feickert, Andrew, C. Burr, J. Watson, F. Rost, A. Pearce, L. Geiger, A. Abdelmotteleb, B. M. Wiedemann, C. Gohlke, Gonzalo, J. Sanders, J. Drotleff, J. Eschle, L. Neste, M. E. Gorelli *et al.*, scikit-hep/iminuit: v2.12.1, https://doi.org/10.5281/zenodo.6788009 (2022).

[35] S. J. Clark, M. D. Segall, C. J. Pickard, P. J. Hasnip, M. I. J. Probert, K. Refson, and M. C. Payne, First principles methods using CASTEP, Z. Kristallogr. Cryst. Mater **220**, 567 (2005).

[36] J. P. Perdew, K. Burke, and M. Ernzerhof, Generalized gradient approximation made simple, Phys. Rev. Lett. **77**, 3865 (1996).

[37] K. Hiebl, C. Horvath, P. Rogl, and M. Sienko, Magnetic properties and structural chemistry of ternary silicides (RE, Th, U)Ru$_2$Si$_2$ (RE = RARE EARTH), J. Magn. Magn. Mater. **37**, 287 (1983).

[38] H. J. Monkhorst and J. D. Pack, Special points for Brillouin-zone integrations, Phys. Rev. B **13**, 5188 (1976).

[39] B. M. Huddart, A. Hernández-Melián, T. J. Hicken, M. Gomilšek, Z. Hawkhead, S. J. Clark, F. L. Pratt, and T. Lancaster, MuFinder: A program to determine and analyse muon stopping sites, Comput. Phys. Commun. **280**, 108488 (2022).

[40] C. Bonhomme, C. Gervais, F. Babonneau, C. Coelho, F. Pourpoint, T. Azais, S. E. Ashbrook, J. M. Griffin, J. R. Yates, F. Mauri, and C. J. Pickard, First-principles calculation of NMR parameters using the gauge including projector augmented wave method: A chemist's point of view, Chem. Rev. **112**, 5733 (2012).

[41] N. Govind, M. Petersen, G. Fitzgerald, D. King-Smith, and J. Andzelm, A generalized synchronous transit method for transition state location, Comput. Mater. Sci. **28**, 250 (2003).

[42] G. P. Srivastava, *The Physics of Phonons* (A. Hilger, Bristol, Philadelphia, 1990).

[43] L. Kantorovich, *Quantum Theory of the Solid State: An Introduction.* (Kluwer Academic Publishers, Dordrecht, 2004).

[44] D. J. Griffiths and D. F. Schroeter, *Introduction to Quantum Mechanics* (Cambridge University Press, Cambridge, 2018).

[45] G. Allodi and R. D. Renzi, A numerical method to calculate the muon relaxation function in the presence of diffusion, Phys. Scr. **89**, 115201 (2014).